CrystEngComm

Accepted Manuscript

ROYAL SOCIETY OF CHEMISTRY

www.rsc.org/crystengcomm

Cite this: DOI: 10.1039/c0xx00000x

www.rsc.org/xxxxxx

ARTICLE TYPE

ZnO nanoplates-induced phase transformation synthesis of composite ZnS/$In(OH)_3$/In_2S_3 with enhanced visible-light photodegradation activity of pollutants

Yun Gu,[a,b] Zhaodi Xu[a,b], Lan Guo[b] and Yiqun Wan*[a,b]**

Received (in XXX, XXX) Xth XXXXXXXXX 20XX, Accepted Xth XXXXXXXXX 20XX
DOI: 10.1039/b000000x

The composite ZnS-$In(OH)_3$-In_2S_3 (ZnO-ZIIS) was synthesized *via* a facile hydrothermal method using ZnO nanoplates as zinc resource. As a comparison, the composite $ZnIn_2S_4$-ZnS was obtained applying zinc chloride as zinc raw material and ZnS-In_2S_3 and $In(OH)_3$-In_2S_3 and In_2S_3 were prepared *via* a hydrothermal process. The products were characterized by X-ray diffractometer (XRD), Scanning electron microscope (SEM), Transmission electron microscope (TEM), Brunauer–Emmett–Teller (BET), Photoluminescence spectrometer (PL) and UV–Vis absorption spectrometer. In the hydrothermal process, ZnO nanoplates change the hydrolysis and sulfuration rate of indium salt, which lead to the products with different composition and microstructure compared to the obtained composite using zinc chloride as zinc raw material instead of ZnO. Photocatalytic activity was evaluated by degradation of Rhodamine B (RhB) under visible light ($\lambda \geq 420$ nm) irradiation. The degradation activity of the obtained product applying ZnO nanoplates as zinc raw material is superior to the other products and is nearly 5 times as high as that of the product synthesized using Zinc chloride as zinc raw material. The enhanced photodegradation activity can be attributed to the extended visible light absorption range, the bigger specific surface area, pore size distribution and the effective photogenerated electron-hole separation due to proper energy-band structure. A possible mechanism is discussed.

1. Introduction

Recently, the photocatalytic degradation of organic pollutants in the presence of semiconductors, especially composite photocatalysts has attracted increasing attention because it is a promising technology and efficient solution for the treatment of waste water.[1-4]The composite photocatalysts can effectively inhibit the recombination of photogenerated carriers and extend the spectrum response compared to single photocatalysts. Some composite photocatalysts based on In_2S_3, such as In_2O_3-In_2S_3[5], TiO_2-In_2S_3,[6] ZnO-In_2S_3[7] and In_2S_3-Graphene[8] have been successfully synthesized and exhibited enhanced photocatalytic activities. In addition, indium hydroxide ($In(OH)_3$) is an important wide-gap semiconductor material with a direct band gap of 5.15 eV. [9] Many researchers have demonstrated that it has the strong oxidation and reduction performances. [10-13] $In(OH)_yS_z$ solid solutions were investigated and their photocatalytic activity were superior to the single In_2S_3 and $In(OH)_3$ under visible light irradiation. [14,15]

The structure, grain size, morphology and composition of photocatalyst depend on the preparation method. The photocatalytic properties of catalysts are closely related to their microstructure, morphology and composition. Fu *et al.* synthesized $ZnSn(OH)_6$ by four different methods, and found that preparation method influenced seriously the microstructure and the photocatalytic performances of the products. [16] Chen *et al.* prepared the heterostructure In_2O_3/$In(OH)_3$ photocatalyst by programmed thermal treatment of $In(OH)_3$. [17] Yu *et al.* controlled the partial phase transformation of AgO from Ag_2CO_3 and synthesized Ag_2O/Ag_2CO_3 heterostructures by regulating calcination temperature and time.[18] Brahma *et al.* deposited tapered ZnO nanorods on Si(100) substrate with different crystallinity, morphology, and optical properties by using newly designed metal–organic complex of zinc as the precursor, and microwave irradiation assisted chemical synthesis as a process. [19] Herein, we developed a simple and novel method for synthesis of composite ZnS-$In(OH)_3$-In_2S_3 *via* applying ZnO nanoplates as zinc raw material to regulate precipitation order and rate of indium ions. Meanwhile, we compared and found the tremendous difference of composition, microstructure and photodegradation activity of the products obtained using different raw materials and preparation procedure. In an acid medium, addition of ZnO nanoplates could change hydrolysis and sulfuration sequence of indium ions under the condition of deficient sulfur source (thioacetamide). The as-obtained composite ZnS-$In(OH)_3$-In_2S_3 with wider pore size distribution, larger BET specific surface area, higher light absorption capacity and proper energy-band structure exhibited extremely high activity, which was vastly

superior to the other products.

2. Experimental

2.1. Preparation of ZnO Nanoplates

The ZnO nanoplates were synthesized by a hydrothermal process at 95 °C for 24 h using a modified literature method.[20] Typically, 40 mmol ZnO, 80 mmol NaOH and 0.014 mmol sodium citrate were dissolved in 75 mL of ultrapure water. The mixture was stirred for 30 min and then transferred to 100 mL Teflon autoclave and treated at 95 °C for 24 h, and then was cooled to room temperature in air. The white product was separated by filtration and washed with ultrapure water, and dried at 70 °C for 6 h.

2.2. Preparation of In_2S_3 photocatalyst

The In_2S_3 photocatalyst was synthesized using $In_2(SO_4)_3$•$6H_2O$ and thioacetamide (TAA) as raw material. In a typical procedure, 0.83 mmol $In_2(SO_4)_3$•$6H_2O$ and 6.0 mmol TAA were dissolved in 75 mL of ultrapure water. The mixture was stirred for 30 min and then transferred to 100 mL Teflon autoclave. The reaction mixture was heated at 120 °C for 6 h and then cooled to room temperature in air. The yellow product was separated by filtration and washed with ultrapure water and ethanol, and dried at 70 °C for 6 h.

2.3. Preparation of ZnS-$In(OH)_3$-In_2S_3 photocatalyst

The ZnS-$In(OH)_3$-In_2S_3 photocatalyst was synthesized *via* a hydrothermal treatment method. Typically, 0.83 mmol $In_2(SO_4)_3$•$6H_2O$, 6.0 mmol TAA and 4.0 mmol ZnO were added in 75 mL of ultrapure water. The mixture was stirred for 90 min and then transferred to 100 mL Teflon autoclave. The reaction mixture was heated at 120 °C for 6 h and then cooled to room temperature in air. The yellow product was separated by filtration and washed with ultrapure water and ethanol, and dried at 70 °C for 6 h.

2.4. Preparation of $ZnIn_2S_4$-ZnS photocatalyst

The $ZnIn_2S_4$-ZnS ($ZnCl_2$-ZIS) photocatalyst was synthesized *via* a hydrothermal treatment method. Typically, 0.83 mmol $In_2(SO_4)_3$•$6H_2O$, 6.0 mmol TAA and 4.0 mmol $ZnCl_2$ were dissolved in 75mL of ultrapure water. The mixture was stirred for 30 min and then transferred to 100 mL Teflon autoclave. The reaction mixture was heated at 120 °C for 6 h and then was cooled to room temperature. The product was separated by filtration and washed with ultrapure water and ethanol, and dried at 70 °C for 6 h.

2.5. Preparation of ZnS-In_2S_3 and $In(OH)_3$-In_2S_3 photocatalysts

As a comparison, ZnS-In_2S_3 and $In(OH)_3$-In_2S_3 visible light photocatalysts were prepared by hydrothermal process with two step. Firstly, the In_2S_3 was prepared according to the experimental 2.2. The next step is similar to the preparation process of the $ZnIn_2S_4$-ZnS ($ZnCl_2$-ZIS) photocatalyst only replacing the $In_2(SO_4)_3$•$6H_2O$ with 0.83 mmol prepared In_2S_3. The preparation of $In(OH)_3$-In_2S_3 is as follows. 75 mL 0.99 mol/L NaOH solution was slowly added to the mixture of 0.67 mmol In_2S_3 prepared according to the experimental 2.2 and 0.16 mmol $In_2(SO_4)_3$•$6H_2O$. The suspension was stirred for 30 min and then transferred to 100 mL Teflon autoclave. The reaction mixture was heated at 120 °C for 6 h and then was cooled to room temperature. The product was separated by filtration and washed with ultrapure water and ethanol, and dried at 70 °C for 6 h.

2.6. Characterization

XRD patterns were acquired on a Bede D1 System multifunction X-ray diffractometer, employing Cu Ka (λ= 1.5418 Å) radiation. Voltage and current were 40 kV and 40 mA, respectively. The scanning electron microscopy (SEM) images were taken on a JSM 6701F field emission scanning electron microscope. The transmission electron microscopy (TEM) images were taken on a JEM-2100 field emission transmission electron microscope working at 200 kV. Brunauer–Emmett–Teller (BET) surface areas were determined by nitrogen adsorption–desorption using a Mircromeritics ASAP 2020C analyzer and the pore size distribution was calculated using Barrett–Joyner–Halenda (BJH) method. UV-Vis diffuse reflectance spectra were obtained on a Hitachi U-4100 spectrophotometer. UV-Vis absorption spectra were obtained on a Shimadzu UV-2501PC spectrophotometer. Fluorescence emission spectra were recorded on a Hitachi F-4500 type fluorescence spectrophotometer with 350 nm excitation source over a wavelength range of 400–600 nm. Total organic carbon (TOC) was determined by GE Sievers 860 TOC analyzer *via* the standard method.[21]

2.7. Photocatalytic Experiments

Photocatalytic reaction was carried out at room temperature in a 400 mL Pyrex cell with an open with a 420 nm cutoff filter to cover the top. A 300 W Xe lamp was used as the light source. In order to maintain a constant room temperature of suspension during visible light irradiation process, a water bath was used. In a typical photocatalytic experiment, 50 mg of the as-prepared photocatalyst was dispersed in 250 mL of the 11.2 mg/L Rhodamine B (RhB) solution. Prior to illumination, the suspension was magnetically stirred in the dark for 1 h to reach adsorption-desorption equilibrium of RhB on the catalyst surface. 5 mL of reaction suspension was sampled at intervals of 5 min, and separated by filter membrane of syringe to remove the catalyst particles. The concentration of RhB in the clear supernatant solution was monitored by measuring the changes in the absorbance at ca. 554 nm. The degradation efficiency of the photocatalysts can be calculated by equator (1):

$$Degradation = (1 - C/C_0) \times 100\% \quad (1)$$

Where C_0 is the concentration of RhB after adsorption equilibrium and C is the residual concentration of RhB at different illumination intervals.

The photodegradation of RhB follows pseudo-first-order kinetics, which can be expressed as

$$\ln(C_0/C) = kT \quad (2)$$

Where k is the degradation rate constant (min^{-1}).

2.8. Determination of Hydroxyl Radicals (•OH)

Hydroxyl radicals (•OH) produced under visible light irradiation were measured by the fluorescence method using terephthalic acid (TA) as a probe molecule. 50 mg of photocatalyst was dispersed in a 100 mL of the 5.0×10^{-4} mol/L terephthalic acid aqueous solution with a concentration of 2.0×10^{-3} mol/L NaOH solution at ambient temperature. The resulting suspension was then exposed to visible light irradiation. 5 mL of suspension was collected at intervals of 5 min and separated by filter membrane of syringe to measure the maximum fluorescence emission intensity with an excitation wavelength of 315 nm. This method relies on the fluorescence signal at 425 nm of the hydroxylation of terephathic acid with •OH generated at the photocatalysts interface. [7, 22]

3. Results and discussion

3.1. XRD analysis

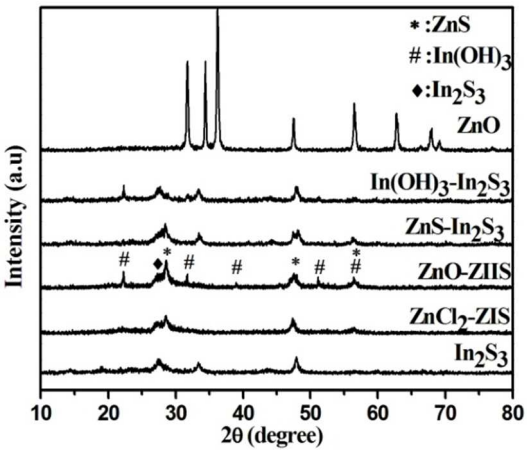

Fig. 1 XRD patterns of the obtained products.

The XRD patterns of the as-prepared products are shown in Fig. 1. the ZnO precursor shows a highly crystalline hexagonal phase of ZnO (JCPDS Cards No. 36-1451). Diffraction peaks of In_2S_3 correspond to tetragonal In_2S_3 (JCPDS Cards No. 73-1366). When using the prepared ZnO as zinc resource, the obtained product (ZnO-ZIIS) is composed of cubic ZnS (JCPDS Card No. 77-2100), cubic $In(OH)_3$ (JCPDS Card No. 85-1338) and tetragonal In_2S_3 (JCPDS Cards No. 73-1366). However, employing zinc chloride as zinc resource, the diffraction peaks of sample $ZnCl_2$-ZIS are consistent with those of cubic ZnS and hexagonal phase $ZnIn_2S_4$ (JCPDS Card No. 65-2023). Despite the molar number of the two kinds of zinc resources is same, diffraction peaks of $In(OH)_3$ and In_2S_3 cannot obviously be observed from the pattern of the $ZnCl_2$-ZIS, which reveal the ZnO precursor can change the composition of the products. As for the sample ZnS-In_2S_3, its diffraction peaks can be attributed to cubic ZnS and tetragonal In_2S_3. The diffraction peaks of $In(OH)_3$-In_2S_3 correspond to the cubic $In(OH)_3$ and tetragonal In_2S_3.

3.2. SEM and TEM analysis

SEM images of the products are shown in the Fig. 2. It can be observed that the ZnO precursor is composed of nanoplates with a wide of *ca.* 50—165 nm, a thickness of *ca.* 16 nm (Fig. 2a). The ZnO-ZIIS is composed of flaky and microspheres particles with a

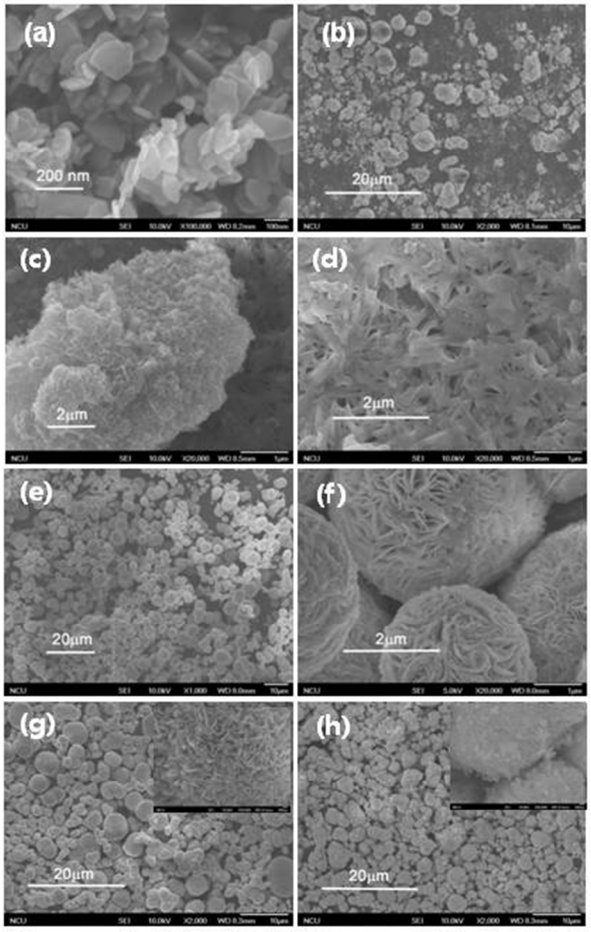

Fig.2 SEM images of the samples (a) ZnO, (b, c, d) ZnO-ZIIS, (e, f) $ZnCl_2$-ZIS, (g) ZnS-In_2S_3, (h) $In(OH)_3$-In_2S_3.

diameter of *ca.* 50 nm—6.0 μm (Fig. 2b). Moreover, as shown in Fig. 2c, Flaky particles are stacked by petal-like nanoplates and particles with square regular shape in accord with the raw material of ZnO. We deduce that the ZnO precursor transformed into ZnS directly through ion exchange reaction between S^{2-} ions and O^{2-} ions. Magnifying the Fig. 2c, we find the ZnO-ZIIS exhibiting irregular pore structure with wide pore size distribution (Fig. 2d). The $ZnCl_2$-ZIS consists of marigold-like microspheres closely assembling with nanoplates, and the particle size of the $ZnCl_2$-ZIS ranges from 1μm to 7 μm (Fig. 2e, f). As shown in the Fig. 2g, the ZnS-In_2S_3 is composed of the microspheres with a diameter of ca. 0.90 — 4.5μm. The inset image of single microsphere shows that the microsphere exhibits a marigold-like superstructure the same as the $ZnCl_2$-ZIS. The Fig. 2h shows the $In(OH)_3$-In_2S_3 is consisted of microspheres and irregular particles with rough surface. And grain size distribution is from several nanometers to 3.5 μm. The inset image shows the rough surface of microsphere is covered by a large number of nanoparticles. Compared with the other obtained samples, the size distribution and morphology of the ZnO-ZIIS is obviously different. The results illustrate the different zinc source and preparation method lead to the formation of the products with different morphologies. The TEM and HRTEM images of the ZnO-ZIIS (a, b) and TEM of the $ZnCl_2$-ZIS (c) are shown in the Fig. 3. When using ZnO nanoplates as zinc resource in the hydrothermal process, the as-

prepared ZnO-ZIIS is composed of nanoplates and nanoparticles which loosely assembled with a large number of pores (Fig. 3a). Whereas the as-synthesized $ZnCl_2$-ZIS using zinc chloride as zinc resource consists of flower-like microspheres closely assembling with nanosheets (Fig. 3c), which verifies the result of BET surface area, pore volume and pore size distribution (Fig. 4, Table 1). The fringes of 0.314 nm and 0.324 nm are corresponding to the (111) plane and (109) plane of ZnS and In_2S_3, respectively, whereas that of 0.398 nm is indexed to the (200) plane of $In(OH)_3$ (Fig. 3b). These results agree with those of XRD (Fig. 1) and SEM (Fig. 2) that employing different zinc resources, the prepared samples hold different composition and morphology.

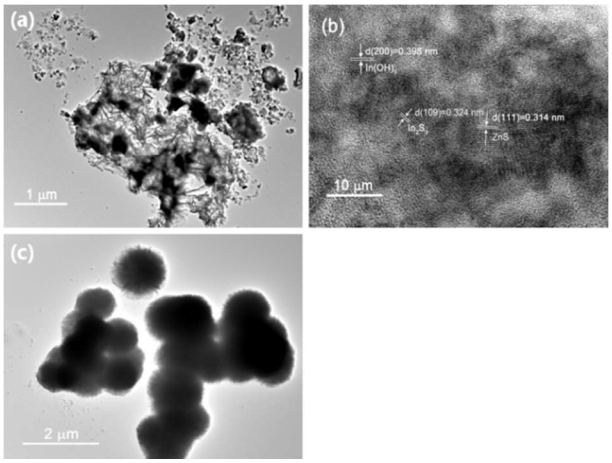

Fig.3 TEM and HRTEM of the ZnO-ZIIS (a, b) and TEM of the $ZnCl_2$-ZIS (c).

3.3. BET surface area and pore size distribution

Table 1 Surface area, Pore volume and Average pore size of the samples.

Sample	Surface area (m^2/g)	Pore volume (cm^3/g)	Average Pore size (nm)
ZnO-ZIIS	43.3	0.171	15.2
$ZnCl_2$-ZIS	8.66	0.0190	8.91
ZnS-In_2S_3	38.0	0.0415	4.37
$In(OH)_3$-In_2S_3	69.2	0.0922	5.33

In order to gain insight into the porosity and the specific surface area of the obtained products, Brunauer-Emmett-Teller (BET) gas-sorption measurement was performed. The results of the surface area, pore volume and average pore size of the products are listed in Table 1. The BET surface area of ZnO-ZIIS is not the largest, but its pore volume and average pore size are the largest among of the products. However, the BET surface area and pore volume of $ZnCl_2$-ZIS are the smallest, but it has larger pore size compared with the ZnS-In_2S_3 and $In(OH)_3$-In_2S_3. The results can be related with the particle size and surface morphology of the products. The nitrogen adsorption–desorption isotherms of the ZnO-ZIIS and $ZnCl_2$-ZIS are displayed in Fig. 4a. They all show hysteresis loops at $P/P_0 > 0.45$. According to the IUPAC classification, [23] it can be seen clearly that the two samples can be classified as typical IV adsorption–desorption isotherms, which correspond to mesoporous solids. Furthermore, the hysteresis loop of the ZnO-ZIIS is type H3, indicating the presence of slit-shaped pores with non-uniform size and shape.[24] The hysteresis loop of the $ZnCl_2$-ZIS is type H4, which is often associated with narrow slit-like pores.[25] Pore size distribution plots of the samples are shown in Fig. 4b. According to the Fig. 4b, the Pore size distribution of the ZnO-ZIIS is wider than that of the $ZnCl_2$-ZIS, which can be proved by SEM and TEM images.

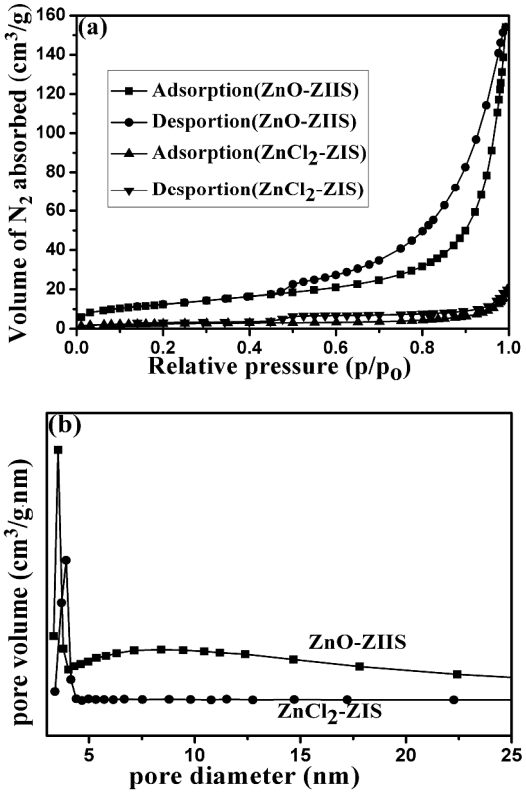

Fig.4 (a) Nitrogen adsorption–desorption isotherms and, (b) pore size distribution curves for the samples calculated on the basis of the BJH equation.

3.4. UV–Vis DRS

The UV-Vis diffuse reflectance spectra (UV-Vis DRS) of the products are shown in the Fig. 5a. All the products can absorb visible light and have steep absorption, which suggest that the absorption is relevant to the band gap due to the intrinsic transition of the samples rather than the transition from impurity levels.[26, 27] The absorption edge of the ZnO-ZIIS has a monotonic red shift compared with the absorption edge of $ZnCl_2$-ZIS. The light absorption capacity of $In(OH)_3$-In_2S_3 is weaker than the other products. It is possibly the reason that a good deal of $In(OH)_3$ nanoparticles cover the In_2S_3 microspheres. Just like the change tendency of absorption curve of the ZnO-ZIIS including $In(OH)_3$.

Moreover, the band gap energy of a semiconductor could be calculated by equator (3): [28]

$$\alpha = K\frac{(h\nu - E_g)^{n/2}}{h\nu} \quad (3)$$

Where α is the absorption coefficient, hν is the photon energy, and K is constant. The n of an indirect band gap is equal to 1 while it is 4 for a direct band gap. The E_g of the samples can be obtained from a plot of $(ah\nu)^2$ versus the photon energy (hν).[29,30] The Fig. 5b shows the plots of $(ah\nu)^2$ versus photo energy for the

band gap energies of the products.

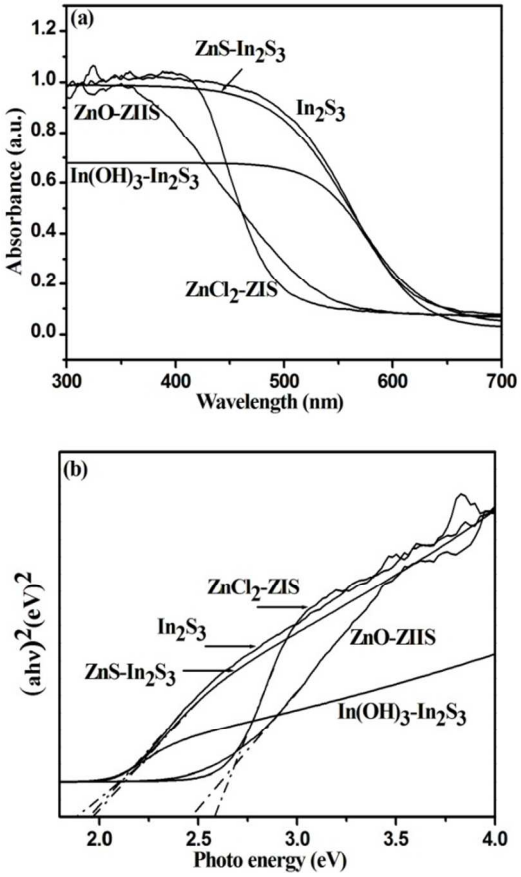

Fig.5 (a) UV-Vis diffuse reflectance spectra of the prepared products. (b) Plots of $(ahv)^2$ versus photo energy for the band gap energies of the prepared products.

The band gaps of all the samples are listed in the Table 2. The band gap energies of ZnS-In_2S_3 and $In(OH)_3$-In_2S_3 are similar to the single In_2S_3, which illustrate the two prepared products might not form heterstructures or compounds. The band gaps of ZnO-ZIIS and $ZnCl_2$-ZIS are larger than that of In_2S_3. Probably because the ZnS or $In(OH)_3$ with wide band gap has formed the heterstructures or compounds with In_2S_3 in the ZnO-ZIIS and $ZnCl_2$-ZIS. According to the intensity and wavelength distribution of the irradiation light employed Xe lamp, [31] the intensity of visible light with a wavelength range from 500 to 600 nm is larger than that of below 500 nm. The Fig. 5a shows the absorption band edges of ZnO-ZIIS and $ZnCl_2$-ZIS are around 560 nm and 500 nm, respectively, and the former has higher absorption capacity than the latter in the wavelength range from 460 to 600 nm. Therefore, the energy of excited light can be utilized sufficiently and much more photogenerated carrier will be generated during the photocatalytic reaction of the ZnO-ZIIS. In this way, the high visible light absorption capacity can make the ZnO-ZIIS more active than the $ZnCl_2$-ZIIS in photocatalytic degradation of RhB.

3.5. Fluorescence emission spectra

The fluorescence emission spectra of the ZnO-ZIIS and $ZnCl_2$-ZIS using an excitation wavelength at 350 nm are shown in Fig. 6. It can be seen that the $ZnCl_2$-ZIS exhibits higher intensity of emission spectra than that of the ZnO-ZIIS. Lower fluorescence emission intensity implies lower electron–hole recombination rate and corresponds to higher photocatalytic activity.[32, 33] In case of the $ZnCl_2$-ZIS, the photoinduced electrons and holes might recombination more rapidly since photogenerated electrons cannot effectively migrate. However, as for the ZnO-ZIIS, the photogenerated carries can easily migrate between In_2S_3 and $In(OH)_3$ due to their matching band potentials and interface interaction, which lead to decrease recombination rate. The results prove that the ZnO-ZIIS with proper energy band structure is helpful to inhibit the recombination of photogenerated carries and improve its photodegradation activity of RhB.

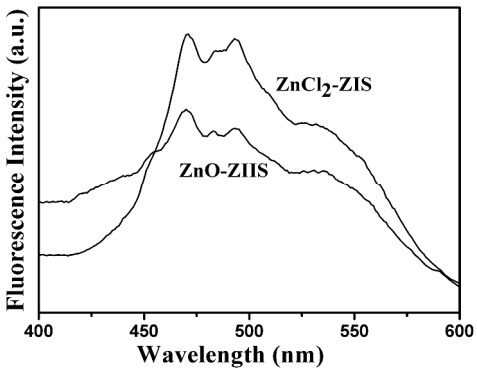

Fig.6 Fluorescence emission spectra of the ZnO-ZIIS and $ZnCl_2$-ZIS.

3.6. Photocatalytic activity for degradation of RhB

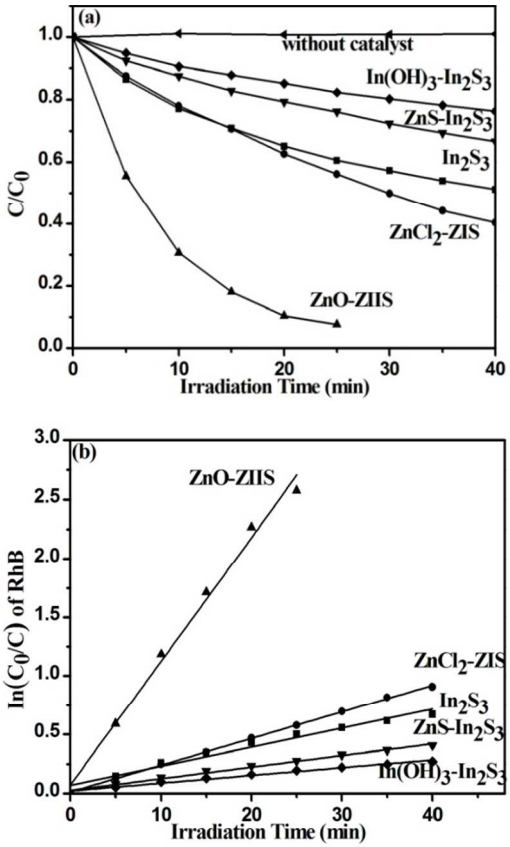

Fig.7 (a) photocatalytic performances of the obtained products and without catalyst for the degradation of RhB solution under visible light, (b) plots of $In(C_0/C)$ as a function of visible light irradiation time for photodegradation of RhB solution containing 50 mg photocatalyst

The performances of the as-prepared photocatalysts in the RhB solution under visible light irradiation are shown in Fig. 7a. According to the Fig. 7a, the RhB self-photolysis without catalyst under visible light irradiation is not observed within 40 min, which indicates that RhB is stable in the absence of photocatalyst under visible light irradiation. RhB removals of the products are listed in the Table 2 under visible light irradiation for 25 min. Fig. 7b shows a linear relationship between $\ln(C_0/C)$ and reaction time, which indicates that the photocatalytic degradation of RhB follows pseudo-first-order kinetics under visible light irradiation. The apparent rate constants are listed in the Table 2. It can be seen that the order of rate constant is as follows: ZnO-ZIIS>$ZnCl_2$-ZIS>In_2S_3>ZnS-In_2S_3>In$(OH)_3$-In_2S_3. The activity of the ZnO-ZIIS is about 4.7 times higher than $ZnCl_2$-ZIS and 6.8 times higher than In_2S_3 for photocatalytic degradation of RhB.

Absorption spectral changes of RhB solution as a function of irradiation time under visible light irradiation in the presence of the ZnO-ZIIS and $ZnCl_2$-ZIS are showed in the Fig. 8. Compared to the RhB solution in the presence of the $ZnCl_2$-ZIS, the absorption peak intensity of RhB solution in the presence of the ZnO-ZIIS at around 544 nm undergoes more obvious decrease with irradiation time. Meanwhile the hypsochromic shifts of the absorption band are considerably insignificant. According to the literature,[34] we deduce the deethylation reaction on the surface of the ZnO-ZIIS and $ZnCl_2$-ZIS is negligible and the main reaction is the cycloreversion of the whole chromophore structure of the RhB molecule over the ZnO-ZIIS and $ZnCl_2$-ZIS.

Table 2 The experimental results of the obtained samples.

Samples	ZnO-ZIIS	$ZnCl_2$-ZIIS	In_2S_3	ZnS-In_2S_3	In$(OH)_3$- In_2S_3
Band gap(eV)	2.47	2.58	1.98	1.99	1.90
decolorization rate of RhB	95.0%[a]	43.8%	39.5%	20.7%	15.8%
Apparent rate constant (k)	0.11[a]	0.023	0.016	0.011	0.0071
mineralization rate of RhB	86.4%[a]	34.3%	13.9%	4.80%	9.70%
Adsorption amount	47.4%	13.8%	26.5%	10.2%	14.7%
Zeta potential (mV)	-21.3	-20.1	-12.1	-29.4	12.4

[a] denoted as illumination for 25 min under visible light, the other samples illumination for 40 min under visible light.

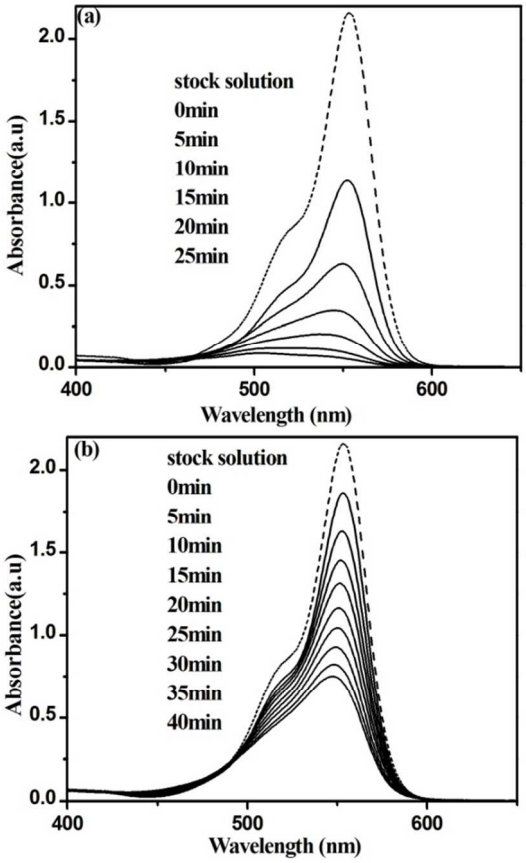

Fig.8 Temporal UV-Vis absorption spectral changes of RhB as a function of irradiation time in the presence of (a) ZnO-ZIIS, (b) $ZnCl_2$-ZIS. Reaction conditions: 250 mL RhB solution, 11.2 mg/L; catalyst 50 mg; 300 W Xe-lamp, $\lambda \geq 420$ nm. (0 min denoted as adsorption-desorption equilibrium and light on)

The total organic carbon (TOC) of the five sample solutions was analyzed. Initial value of 7.80 mg/L for stock solution was obtained for TOC, TOC values of the sample solutions for ZnO-ZIIS, $ZnCl_2$-ZIS, In_2S_3, ZnS-In_2S_3 and In$(OH)_3$-In_2S_3 were 1.06, 5.12, 6.71, 7.50, 7.04, respectively. Mineralization rate of RhB for ZnO-ZIIS is more much larger than that of the other samples. From the TOC results, the mineralization rates of RhB are listed in the Table 2. The results reveal the degradation of RhB dye chromophore followed by partial re-mineralization of degradation products might have occurred.[35]

To explore the relationship between the adsorption capacity of the obtained products and their photoactivity, the 11.2 mg/L Rhodamine B (RhB) solution containing 50 mg catalysts was stirred for 1 h in the dark. The adsorption amounts of the products are listed in the Table 2. The adsorption capacity of ZnO-ZIIS is the biggest, and that of ZnS-In_2S_3 is the lowest. Adsorption capacity usually attributes to the surface electric property and BET surface area of the catalyst. Because the RhB molecule is positively charged in solution, according to electrostatic interaction theory, more negative charge on the surface of photocatalyst will improve the adsorption of RhB molecules. To find out the reason of higher adsorption capacity of the ZnO-ZIIS, the Zeta potentials of the samples were carried out. The Zeta potentials of the products are listed in the Table 2. The In$(OH)_3$-In_2S_3 with positive charge has bigger adsorption capacity than the $ZnCl_2$-ZIIS and ZnS-In_2S_3 with negative charge, which illustrates the adsorption capacity mainly depends on the surface area and pore volume of products.

In general, the active radicals are very important in the photodegradation process. Hydroxyl radical (•OH), with the high oxidative ability enough to attack many organic molecules, is regarded as a key active species in the photocatalytic process.[36,37] In order to confirm the existence of •OH, the formed hydroxyl radicals (•OH) on the surface of photocatalysts illuminated by visible light are detected by PL technique. The PL emission spectra from terephthalic acid (TA) solution excited at 315 nm in

the presence of the ZnO-ZIIS and $ZnCl_2$-ZIS under visible light irradiation for 25 min are shown in Fig. 9. The emission peak intensity of the TA solution at 425 nm increases gradually with increasing irradiation time in the presence of the two photocatalysts ZnO-ZIIS and $ZnCl_2$-ZIS, indicating that •OH is increasingly formed during the photocatalytic process under visible light irradiation. However, under the visible light illumination for equal times, the PL intensity of TA solution in the presence of the ZnO-ZIIS is greatly higher than that of the $ZnCl_2$-ZIS. The photocatalytic activity has a positive correlation with the formation rate of •OH radicals. The result proves that the ZnO-ZIIS has higher generating ability of •OH, so that it has the higher photocatalytic activity than $ZnCl_2$-ZIS.

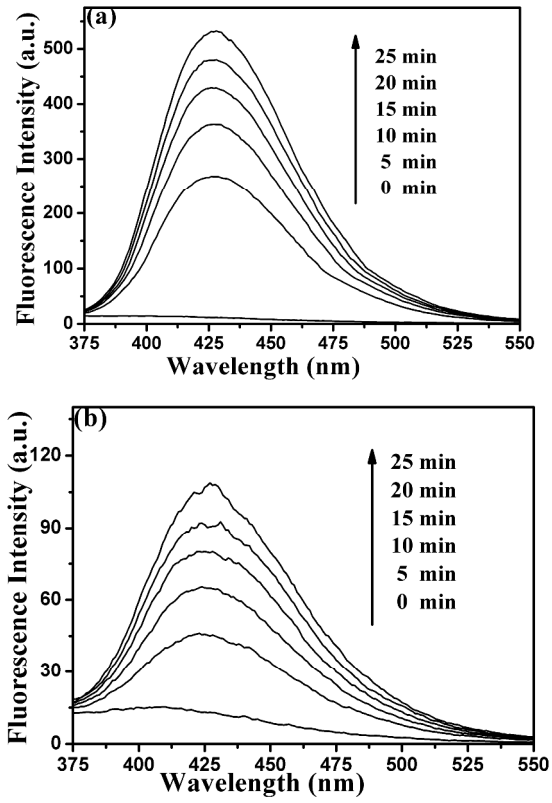

Fig.9 Fluorescence spectral of terephthalic acid solution excited at 315 nm in the presence of (a) ZnO-ZIIS and (b) $ZnCl_2$-ZIS at different illumination time.

3.7. Mechanism

In order to explore evolution process of the composition, grain size and morphology of the as-prepared ZnO-ZIIS during the hydrothermal treatment, the samples obtained at the different hydrothermal time were characterized applying XRD and SEM technology. The XRD patterns of the products are showed in the Fig.10. The preparation of the product obtained before hydrothermal treatment was as follows (0 h): 4.0 mmol ZnO and 0.83 mmol $In_2(SO_4)_3$•$6H_2O$ were added into the 75 mL 0.080 mol/L thioacetamide solution and stirred for 30 min, then the mixture were filtered, wished and dried. As shown in the Fig. 10a, the diffraction peaks intensities of ZnO obviously decline and an amorphous peak in the range of 20^0-30^0 appears, which suggest decrease of ZnO nanoplates crystallization and formation of amorphous species under the experimental condition. After hydrothermal treatment for 0.5 h (Fig. 10b), diffusion peaks of $In(OH)_3$ and ZnS obviously occur and diffusion peak intensities of ZnO decrease increasingly, which illustrate the as-prepared samples concluding ZnS, $In(OH)_3$ and ZnO.

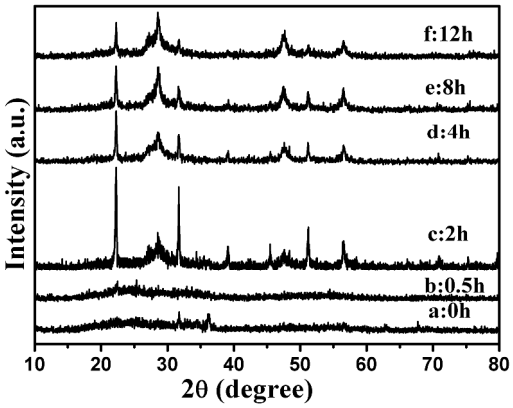

Fig.10 XRD patterns of the products synthesized at the different reaction time.

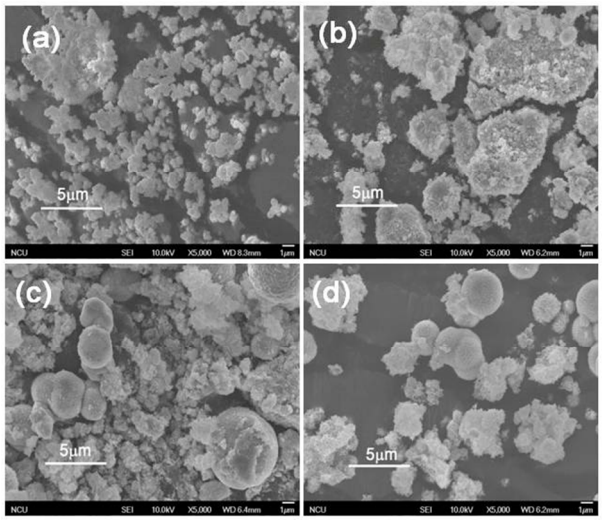

Fig.11 SEM images of ZnO-ZIIS (a) 0.5h, (b) 4h, (c) 8h, (d) 12h.

According to the literature, [38] when the molar ratio of indium to thioacetamide is 1:2, the as-synthesized sample is composed of $In(OH)_3$ and In_2S_3. It suggests the reaction process between indium salt and organic sulfur source is not a simple precipitant reaction between In^{3+} and S^{2-}. Thioacetamide (TAA) in an acid medium (Eq. (4)) hydrolyzes into NH_4^+ and thioacteic acid (CH_3CSOH).[39] Then the CH_3CSOH further hydrolyzes into H_2S. Therefore the process of hydrolysis of TAA and release of H_2S is slow. In comparison with the TAA hydrolysis and release rate of H_2S, the solution pH value controls precipitation process of the product in an acid medium.[40] pH value of our hydrothermal reaction system was determinate to 3.5. We deduce that at the initial stage most indium ions hydrolyze into $In(OH)_3$ (Eq. (5)) and only little In_2S_3 is produced (Eq. (6)). With the reaction time increase, the concentration of H_2S gradually increases. Because the solubility product constant (K_{sp}) of ZnO (6.8×10^{-17}) is much larger than that of $In(OH)_3$ (1.3×10^{-37}) and In_2S_3 (5.7×10^{-74}), [41] ZnO nanoplates in an acid medium react with H_2S and then ZnS

species are generated and grow up during the Ostwald-ripening process (Eq. (7)). Therefore XRD patterns suggest the diffusion peaks of ZnS strengthen. Heretofore 2h, the diffusion peaks intensities of $In(OH)_3$ maximize. The disappearance of characteristic peaks of ZnO demonstrates that the ZnO nanoplates are wholly transformed to ZnS (Fig. 10c). TAA was continuously decomposed into H_2S. Since the solubility product constant (K_{sp}) of $In(OH)_3$ (1.3×10^{-37}) is far larger than that of In_2S_3 (5.7×10^{-74}). Indium ions (In^{3+}) from $In(OH)_3$ partial ionization react with H_2S and form more stable In_2S_3, which result in the decrease of diffusion peak intensity of $In(OH)_3$ (Fig. 10d, e, f). According to the stoichiometric ratio of ZnS and In_2S_3, the amount of the added TAA is insufficient to fully form ZnS and In_2S_3. Therefore the final product is composed of ZnS, $In(OH)_3$ and In_2S_3 (as shown in Fig. 1). The SEM images of the products obtained during different hydrothermal treatment time are shown in the Fig. 11. The Fig. 11a shows the sample obtained by hydrothermal treatment for 0.5 h, consists of uniform spherical particles with a diameter of about 0.5 μm. However, the samples acquired after 4 h are similarly assembled with flower-like microspheres and sheet-like grains with irregular morphology (Fig. 11b, c, d). When using $ZnCl_2$ as zinc raw material instead of ZnO, Zn^{2+} and In^{3+} ions can react with H_2S and produce $ZnIn_2S_4$, and residual Zn^{2+} ions precipitate into ZnS in the reaction system including Cl^- ions. [27,42] (Fig. 1)

$$CH_3CSNH_2 \xrightarrow{H_3O^+} \begin{cases} NH_4^+ \\ CH_3CSOH + H_2O \rightarrow CH_3COOH + H_2S \end{cases} \quad (4)$$

$$In^{3+} + 3H_2O \rightarrow In(OH)_3 + 3H^+ \quad (5)$$

$$2In^{3+} + 3H_2S \rightarrow In_2S_3 + 6H^+ \quad (6)$$

$$ZnO + H_2S \rightarrow ZnS + H_2O \quad (7)$$

It is well-known that the separation of photoexcited electrons and holes and the amount of photoexcited active species are responsible for the photodegradation activity of catalysts. For the composite photocatalysts, two prerequisites for electron transfer are the electron density diversity and the energy gap of the composite semiconductor materials.[43] The potentials of conduction band (CB) of $In(OH)_3$, In_2S_3 and ZnS are -0.80 eV, -0.93 eV and -1.04 eV (*vs* NHE), respectively.[17,35] In_2S_3 with narrow band gap energy (1.98 eV in this work) can be easily excited and generate electrons and holes under vi sible light illumination. As shown in the Fig. 12, since the CB of In_2S_3 nanosheets is more negative than that of $In(OH)_3$, the photogenerated electrons can transfer from the CB of In_2S_3 to the CB of $In(OH)_3$ and the photogenerated holes are left in the valance band (VB) of the In_2S_3. This electron transfer can reduce the recombination of hole–electron pairs, which is beneficial for improving the photocatalytic efficiency. But as for $In(OH)_3$-In_2S_3, according to its preparation procedure, $In(OH)_3$ species on surface of In_2S_3 particles were rapidly formed by precipitation reaction of In^{3+} and OH^- before hydrothermal treatment, which possibly leads to the weak interface interaction between $In(OH)_3$ and In_2S_3 particles. Therefore the photogenerated electrons cannot effectively transfer from the CB of In_2S_3 to the CB of $In(OH)_3$.

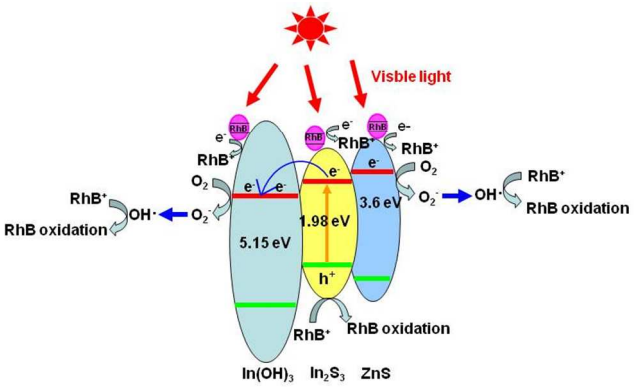

Fig.12 Postulate mechanism of the visible light-induced photodegradation of RhB with composite ZnO-ZIIS.

The above experimental results indicate the as-prepared ZnO-ZIIS has stronger adsorption ability of RhB. The Fig. 8 indicates the RhB molecular can be excited by ca. 540 nm irradiation. The photodegradation process of RhB on the surface of the ZnO-ZIIS catalyst under visible light is shown in the Fig. 12. When the RhB molecules are adsorbed on the surface of the ZnO-ZIIS, the adsorbed RhB molecules are excited by visible light and inject the electrons to the conduction band of the photocatalyst (Eq. (8)). Since the potential of the valance band of In_2S_3 (1.05 eV) is more negative than the E (•OH/OH^-) (2.38 eV *vs* NHE), E (•OH/H_2O) (2.27 eV *vs* NHE) and the oxidation potential of water (1.23 eV *vs* NHE), h^+_{vb} in the valance band of In_2S_3 cannot oxidize water molecules to form •OH. In our work, the •OH may mainly be produced by O_2 capturing photogenerated electrons to form hydrogen peroxide (Eq. (8-14)).[12, 44] In the end, the excited RhB cationic radicals are oxidized by photogenerated holes and hydroxyl radical into the final products (Eq. (15)).

$$RhB + catalyst + h\nu \rightarrow RhB^+ + catalyst(e^-) \quad -1.09V \quad (8)$$

$$O_2 + e \rightarrow O_2^- \quad -0.33V \quad (9)$$

$$H^+ + O_2 + e \rightarrow HO_2 \quad -0.037V \quad (10)$$

$$2H^+ + O_2 + 2e \rightarrow H_2O_2 \quad +0.69V \quad (11)$$

$$2H^+ + O_2^- + e \rightarrow H_2O_2 \quad +1.71V \quad (12)$$

$$H^+ + HO_2 + e \rightarrow H_2O_2 \quad +1.42V \quad (13)$$

$$H_2O_2 + h\nu \rightarrow \bullet OH + \bullet OH \quad (14)$$

$$RhB^+ + h^+ + \bullet OH \rightarrow CO_2 + H_2O + \text{mineral acid} \quad (15)$$

In a conclusion, the higher photodegradation activity of the ZnO-ZIIS attributes to its superior adsorption property and proper energy gap structure.

4. Conclusions

In summary, the ZnS-$In(OH)_3$-In_2S_3 (ZnO-ZIIS) was successfully fabricated by induction of ZnO nanoplates under hydrothermal condition. In comparison to the samples obtained by different zinc source and preparation method, the ZnO-ZIIS exhibited higher photocatalytic activity for degradation of RhB under visible light illumination. The enhanced activity was attributed to the composition and microstructure of composite ZnS-$In(OH)_3$-In_2S_3. Moreover, the formation and photogenerated carriers transiton mechanism of the ZnO-ZIIS was explored. This work is important to understanding the complex hydrothermal process to fabricate multi-component materials for photocatalytic application.

Acknowledgements

The financial support of this study from National Key Technology R&D Program of the "12th Five-Year Plan" (2012BAK17B02), the Key Technology R&D Program of Jiangxi Province (20133ACG70002), the Research Program of State Key Laboratory of Food Science and Technology in Nanchang University (SKLF-ZZA-201302),the Research Program of State Key Laboratory of Food Science and Technology in Nanchang University (SKLF-ZZB-201304) and the National Nature Science Foundation of China (21366022), are gratefully acknowledged.

Notes and references

* *Corresponding author. Tel./Fax: +86 791 88321370. E-mail: yqwanoy@sina.com (Y. Wan)*
** *Corresponding author. Tel./Fax: +86 791 88304414. E-mail: xuzhaodi@ncu.edu.cn (Z. Xu)*
[a] *State Key Laboratory of Food Science and Technology, Nanchang University, Nanchang 330047, China*
[b] *Center of Analysis and Testing, Nanchang University, Nanchang 330047, China*

1 A. Fujishima, K. Honda, *Nature*, 1972, **238**, 37–38.
2 Z. Zou, J. Ye, K. Sayama, H. Arakawa, *Nature*, 2001, **414**, 625–627.
3 W. Yao, C. Huang, N. Muradov, A. T-Raissi, *Int. J. Hydrogen Energy*, 2011, **36**, 4710–4715.
4 H. Tong, S. Ouyang, Y. Bi, N. Umezawa, M. Oshikiri, J. Ye, *Adv. Mater.*, 2012, **24**, 229−239.
5 X. Yang, J. Xu, T. Wong, Q. Yang, C. Lee, *Phys. Chem. Chem. Phys.*, 2013, **15**, 12688-12693.
6 X. Gan, X. Li, X. Gao, J. Qiu, F. Zhuge, *Nanotechnology*, 2011, **22**, 305601−305607.
7 S. Khanchandani, S. Kundu, A. Patra, A.K. Ganguli, *J. Phys. Chem. C*, 2013, **117**, 5558–5567.
8 M. Yang, B. Weng, Y. Xu, *Langmuir*, 2013, **29**, 10549–10558.
9 H. Zhu, X. Wang, F. Yang, X. Yang, *Cryst. Growth Des.*, 2008, **8**, 950-956.
10 T. Yan, X. Wang, J. Long, P. Liu, X. Fu, G. Zhang, X. Fu, *J. Colloid Interface Sci.*, 2008, **325**, 425–431.
11 H. Cao, H. Zheng, K. Liu, R. Fu, *Cryst. Growth Des.*, 2010, **2**, 597–601.
12 J. Guo, S. Ouyang, T. Kako, J. Ye, *Appl. Surf. Sci.*, 2013, **280**, 418−423.
13 S. Avivi, Y. Mastai, A. Gedanken, *Chem. Mater.*, 2000, **12**, 1229-1233.
14 Z. Li, T. Dong, Y. Zhang, L. Wu, J. Li, X. Wang, X. Fu, *J. Phys. Chem. C*, 2007, **111**, 4727–4733.
15 Z. Lei, G. Ma, M. Liu, W. You, H. Yan, G. Wu, T. Takata, M. Hara, K. Domen, C. Li, *J. Catal.*, 2006, **237**, 322–329.
16 X. Fu, D. Huang, Y. Qin, L. Li, X. Jiang, S. Chen, *Appl. Catal. B: Environ.*, 2014, *148*, 532-542.
17 J.L. Ewbank, L. Kovarik, C.C. Kenvin, C. Sievers, *Green Chemistry*, 2014, **16**, 865-896.
18 S. Chen, X. Yu, H. Zhang, W. Liu, *J. Hazard. Mater.*, 2010, **180**, 735–740.
19 C. Yu, G. Li, S. Kumar, K, Yang, R. Jin, *Adv. Mater.*, 2014, **26**, 892-898.
20 E.S. Jang, J.H. Won, S.J. Hwang, J.H. Choy, *Adv. Mater.*, 2006, **18**, 3309–3312.
21 Standard methods for the examination of water and wastewater, Method 5310 B.High temperature combustion method, 21st edition, American Public Health Association (APHA), American Water Works Association (AWWA), Water Environment Federation (WEF), Washington, DC, 2005, pp. 5–21.
22 J. Yu, Q. Xiang, M. Zhou, *Appl. Catal. B: Environ.,* 2009, **90**, 595–602.
23 K.S.W. Sing, D.H. Everett, R.A.W. Haul, L. Moscou, R.A. Pierotti, J. Rouquerol, T. Siemieniewska, *Pure Appl. Chem.*, 1985, **57**, 603-619.
24 J.S. Valente, F. Tzompantzi, J. Prince, J.G.H. Cortez, R. Gomez, *Appl. Catal. B: Environ.,* 2009, **90**, 330–338.
25 H. Adelkhani, M. Ghaemi, M. Ruzbehani, *Int. J. Electrochem. Sci.*, 2011, **6**, 123-135.
26 J. Tang, J. Ye, *J. Mater. Chem.*, 2005, **15**, 4246–4251.
27 Z. D. Xu, Y. X. Li, S. Q. Peng, G. X. Lu, S. B. Li, *RSC Adv.*, 2012, **2**, 3358–3366.
28 D.P. Singh, N.R. Neti, A.S.K. Sinha, O.N. Srivastava, *J. Phys. Chem. C*, 2007, **11**, 1638-1645.
29 H. Wei, S. Chen, X. Ren, B. Qian, Y. Su, Z. Yang, Y. Zhang, *CrystEngComm*, 2012, **14**, 7408-7414.
30 S. Liu, X. Wang, K. Wang, R. Lv, Y. Xu, *Appl. Surf. Sci.*, 2013, **283**, 732–739.
31 J. Tang, Y. Liu, H. Li, Z. Tan, D. Li, *Chem. Commun.*, 2013, **49**, 5498-5500.
32 H. Tang, K. Prasad, R. Sanjines, P.E Schmid, F Lévy, *J. Appl. Phys.*, 1994, **75**, 2042-2047.
33 J. Cao, B. Luo, H. Lin, B. Xu, S. Chen, *J. Hazard. Mater.*, 2012, **217**, 107-115.
34 J. Zhuang, W. Dai, Q. Tian, Z. Li, L. Xie, J. Wang, P. Liu, *Langmuir*, 2010, **26**, 9686–9694.
35 Y. Xie, F. Chen, J. He, J. Zhao, H. Wang. *J. Photochem. Photobiol. A*, 2000, **136**, 235–240.
36 X. Zhang, X. Li, C. Shao, J. Li, M. Zhang, P. Zhang, K. Wang, N. Lu, Y. Liu, *J. Hazard. Mater.*, 2013, **260**, 892–900.
37 D.F. Ollis, C.Y. Hsiao, L. Budiman, C.L. Lee, *J. Catal.*, 1984, **88**, 89–96.
38 L. Chen, Z. Zhang, W. Wang, *J. Phys. Chem. C*, 2008, **112**, 4117–4123.
39 O.M. Peeters, C.J. de Ranter, *J. Chem. Soc. Perkin Trans.,* 1974, **2**, 1832–1835.
40 R. Bayón, J. Herrero, *Thin Solid Films*, 2001, **387**, 111-114.
41 H. Stephen, T. Stephen, Solubilities of Inorganic and organic Compounds, Vol 1, Part 1, Pergamon Press: Oxford,1963.
42 Z. D.Xu, Y. X. Li, S. Q. Peng, G. X. Lu, S. B. Li, *CrystEngComm*, 2011, **13**, 4770-4776.
43 S.M. Sze, K.N. Kwok, Physics of Semiconductor Devices, third ed., Wiley, NewYork, 2007
44 Y. A. Ilan, G. Czapski, D. Meisel, *Biochim. Biophys. Acta*,1976, **430** , 209–224.